Plasma-catalytic conversion of CO_2 to CO over binary metal oxide catalysts at low temperatures

Bryony Ashford[1,2], Yaolin Wang[1], Chee-Kok Poh[2], Luwei Chen[2,3], Xin Tu[1*]*

[1]Department of Electrical Engineering and Electronics, University of Liverpool, Liverpool, L69 3GJ, UK

[2]Institute of Chemical and Engineering Sciences, Agency for Science, Technology and Research, 1 Pesek Road, Jurong Island, 627833, Singapore

[3]Department of Materials Science and Engineering, National University of Singapore, 9 Engineering Drive 1, 117576, Singapore

Corresponding authors

Prof. Luwei Chen, E-mail: chen_luwei@ices.a-star.edu.sg

Prof. Xin Tu, E-mail: xin.tu@liverpool.ac.uk

Abstract

Non-thermal plasma (NTP) technology is gaining increasing interest for CO_2 conversion due to its potential to convert inert and stable CO_2 to value-added fuels and chemicals at ambient conditions. Combining catalysts with plasma can enhance conversion and energy efficiency simultaneously, overcoming the trade-off barrier commonly present in plasma processes. This work reports the influence of various ceria-promoted iron oxide catalysts on the decomposition of CO_2 to carbon monoxide and oxygen in a packed bed, dielectric barrier discharge (DBD) reactor at low temperatures and ambient pressure. As ceria is an expensive rare earth metal, its combination with a cheap, abundant metal such as iron can make the process far more economical. The optimum CO_2 conversion (24.5%) and energy efficiency (13.6%) were achieved using γ-Al_2O_3 supported 5Fe5Ce, almost twice the conversion attained using 10Fe (13.3%). Catalysts were characterized using N_2 adsorption, X-ray diffraction (XRD), Raman spectroscopy, H_2-temperature programmed reduction (H_2-TPR), X-ray photoelectron spectroscopy (XPS) and X-ray absorption near edge structure (XANES) analysis. A solid solution formed from the mixture of iron oxide and ceria. A critical concentration of iron oxide is required to increase the number of oxygen vacancy sites in the solid solution. The synergy between Fe and Ce, and thus the oxygen vacancy sites, can also be optimized via the synthesis method. A reaction mechanism has been proposed for CO_2 conversion at the catalyst surfaces.

Keywords*: Non-thermal plasmas; Dielectric barrier discharge; Plasma catalysis; CO_2 conversion; Binary metal oxide catalysts*

1. Introduction

Carbon dioxide (CO_2) capture and utilization (CCU) have received increasing interest due to the dual benefits this process can bring. Firstly, the reduction of carbon dioxide in the atmosphere is paramount to reducing global warming and climate change; secondly, carbon dioxide can be used as a feedstock to produce valuable fuels and chemicals.[1] One such attractive process is the dissociation of CO_2 to CO, which is a very important chemical feedstock for the synthesis of a range of synthetic fuels and platform chemicals.

High temperatures (>1200 °C) are often required to thermally decompose carbon dioxide into carbon monoxide and oxygen (equation 1) as carbon dioxide is a very stable molecule. This thermodynamically unfavourable process results in high energy consumption and low efficiency as the entire reactor volume has to be heated; thus not all energy transferred to the reactor will take part in CO_2 activation.

$$CO_2\ (g) \rightarrow CO\ (g) + \frac{1}{2}O_2\ (g) \qquad \Delta H = 279.8\ kJ/mol = \ 2.9\ eV \tag{1}$$

Non-thermal plasma (NTP) has been regarded as a promising and emerging alternative to conventional thermal catalytic processes for the conversion of CO_2 to higher value fuels and chemicals at low temperatures and ambient pressure.[2–4] The main advantage of using NTP is its non-equilibrium characteristic. This results in a discharge containing electrons with a mean electron energy between 1 and 10 eV, the optimum range for exciting molecular and atomic species and breaking chemical bonds, whilst the bulk gas can be as low as room temperature. This means carbon dioxide can be activated at ambient pressure without the need to heat the entire reactor, which can result in increased energy efficiencies in comparison to thermal or catalytic processes requiring high temperature and/or high pressure. In addition, non-thermal plasma processes can be

63 switched on and off quickly and have the flexibility to be combined with renewable energy sources
64 such as wind power or solar power, especially during peak production of renewable energy, which
65 is prone to fluctuate. Therefore, non-thermal plasma is an effective process for chemical energy
66 storage. CO_2 dissociation has been investigated using microwave discharges,[1,5] glow discharges,[6]
67 radio-frequency discharges[7] and dielectric barrier discharges (DBDs).[8] However, the trade-off
68 between the conversion and energy efficiency has been considered one of the major challenges in
69 current plasma processes, limiting the use of these processes on an industrial scale.[9] The
70 combination of non-thermal plasma with an appropriate catalyst has great potential to tackle this
71 challenge and has been shown to successfully utilize CO_2 through a variety of plasma-catalytic
72 reactions.[8,10–12] The CO_2 conversion can be increased through chemical effects,[13] whilst plasma
73 can change the catalyst properties, which can be beneficial on the catalyst performance.[14–16]
74 Furthermore, the presence of the catalyst can also induce physical changes in the plasma to enhance
75 the energy efficiency of the plasma process.[13] Thus as well as the combined effect from both
76 plasma and catalyst, a synergistic effect can occur as a result of the interaction between the two
77 components which is greater than the sum of the plasma-alone process and the catalytic process.[8]
78 This synergistic effect has been demonstrated in our previous works for CO_2 dissociation in a DBD
79 reactor combined with $BaTiO_3$ or TiO_2.[8]
80
81 Although great efforts have been concentrated on direct conversion of CO_2 to CO and oxygen
82 using different non-thermal plasma systems, far less has been done on the hybrid plasma-catalytic
83 process for CO_2 dissociation to overcome the trade-off between the conversion and energy
84 efficiency of plasma-only processes due to limited knowledge available for selecting efficient and
85 appropriate catalysts for this challenging reaction at low temperatures. Catalysts which are

proficient in similar thermal reactions are often used as a starting point. However, up until now, only a few catalysts have been evaluated for the conversion of CO_2 to CO in plasma reactors.[9,17–19] Van Laer and Bogaerts demonstrated that introducing a ZrO_2 packing into a DBD reactor enhanced the CO_2 conversion and energy efficiency up to a factor of 2.1 and 1.9, respectively, compared to that using a DBD reactor without packing. [20] Zhang et al. investigated the influence of a Ni/SiO_2 catalyst on CO_2 conversion in a DBD reactor packed with either $BaTiO_3$ or glass beads.[18] Chen et al. reported that placing a NiO/TiO_2 catalyst in the downstream of a microwave plasma enhanced the conversion of CO_2 and energy efficiency[21], while Spencer's work showed that the presence of a Rh/TiO_2 catalyst in the downstream of a microwave discharge had a negative effect on CO_2 conversion due to the reverse reaction to reform CO_2 caused by the high temperature microwave plasma[22]. Ceria has been reported to show good activity for a variety of thermal reactions,[23,24] including dissociation of CO_2,[25,26] as it can switch between Ce^{4+} and Ce^{3+} states relatively easily.[27–30] Iron oxide has also been reported to successfully thermally dissociate CO_2 due to the creation of oxygen defect sites as Fe^{3+} is reduced to Fe^{2+}.[31] On the other hand, reduction of metal oxides has been shown to be possible in plasma due to the present of a variety of chemically reactive species including energetic electrons and excited species.[32] In previous works, the increase in CO_2 conversion and energy efficiency achieved in the plasma-catalytic CO_2 dissociation process in comparison to the plasma-alone process for $BaTiO_3$ and TiO_2 catalysts was attributed to the ability of Ti to switch between Ti^{4+} and Ti^{3+} states and the formation of oxygen vacancy on the catalysts surfaces;[8] hence iron oxide and cerium oxide have been selected due to their redox properties.

Combining metal oxides, such as ceria and iron oxide, has been shown to lead to high catalytic performance in thermal processes due to the interactions between the two metals.[23,33,34] However, the properties and reaction performance of Fe/Ce binary oxide catalysts in low temperature plasma-catalytic CO_2 conversion processes have not been reported yet. It is largely unknown how these binary metal oxides especially the change of metal oxide ratio and metal oxide loading order affect the conversion of CO_2 at low temperatures under plasma environment. As such, significant works are required to gain new insights into the synergy of ceria and iron oxide and the role of their interactions in the formation of oxygen vacancy on the catalyst surfaces to achieve high CO_2 conversion using plasma.

In this work, direct conversion of CO_2 to CO and O_2 over Fe/Ce binary oxide catalysts has been carried out in a coaxial DBD reactor at low temperatures and ambient pressure. The influence of Fe/Ce ratio and metal loading sequence on the change of the catalyst structure and properties, and the resulting effects on the conversion of CO_2 and energy efficiency, has been investigated. In addition, a comparison of the fresh and plasma treated catalysts has been performed to better understand the reduction characteristics of the catalysts in the low temperature plasma. Comprehensive catalyst characterization techniques have been used to get new insights into the formation of oxygen vacancies resulting from the interaction of ceria and iron oxide and their links to the conversion of CO_2 at low temperatures.

2. Experimental

2.1 Catalyst synthesis

All catalysts were supported on 1 mm γ-Al_2O_3 beads. The catalysts were prepared via the wetness impregnation method, starting from the nitrate forms of the metal oxides $Fe(NO_3)_3 9H_2O$ (Alfa Aesar, 98.0-101.0% purity) and $Ce(NO_3)_3 6H_2O$ (Sigma Aldrich, 99.99% purity). The catalysts were dried overnight at 110 °C before undergoing calcination at 500 °C for 5 hours. 10 wt.% of the total metals (Fe and Ce) were loaded on the γ-Al_2O_3 support. The metal oxide catalysts shall be referred to using the weight ratio: 10Fe, 7Fe3Ce, 5Fe5Ce, 3Fe7Ce, 10Ce. The 5Fe5Ce catalyst was also prepared via sequential loading of the metals, loading Ce onto the alumina support first followed by calcination for 5 hours at 500 °C, then loading Fe onto this and repeating the calcination step, and vice versa. The catalysts shall be referred to as 5Fe5Ce(Ce) for the former and 5Fe5Ce(Fe) for the latter. All catalysts were dried at 80 °C overnight prior to each experiment.

2.2 Catalyst characterization

The surface area, pore volume and pore size of each catalyst was determined using Brunauer-Emmett-Teller (BET) analysis. A Micromeritics BET Surface Area Analyser was used to determine these properties. N_2 was used as the adsorptive and pore size and volume were found from the BJH desorption curve. The degas temperature was 200 °C with a duration of 24 hours.

Powder x-ray diffraction (XRD) was performed on the samples after calcination in order to identify the phases present. Profiles were produced in the range 2θ = 20-90 ° at a step width of 0.05°. The system used was a Bruker AXS, which used Cu Kα radiation at a wavelength of 0.154 nm.

In order to further investigate the structure of the catalysts, Raman spectroscopy was conducted on the surface of the 10Fe, 5Fe5Ce and 10Ce catalyst beads. A Bruker Senterra Raman microscope

was used for analysis at room temperature using a 50x objective at an excitation wavelength of 514.5 nm and 1 mW power.

Fresh calcined catalysts were analysed using H_2 temperature programmed reduction (H_2-TPR) to reveal the differences in reducibility of the catalysts. 0.2 g of catalyst was used for each reduction. A Thermo Scientific TPROD 1100 was used with a temperature increase from 30 to 800 °C at a heating rate of 10 °C/min in 5 vol.% H_2/Ar flow with a total flow rate of 50 ml/min. No-pre-treatment was carried out.

The oxidation state of the catalysts was analyzed by x-ray photoelectron spectroscopy (XPS) using a VG ESCALAB250. Spent catalysts were transferred under Ar atmosphere to limit re-oxidation in air. The photon source used was Al Kα twin anode with energy of 1486.68 eV and 15000 volts. The step size was 0.05 eV with a dwell time of 0.05 s. Carbon peak C1s with binding energy of 284.5 was used as a standard to correct binding energies in the catalyst spectra.

X-ray absorption near edge structure (XANES) analysis was carried out at the Ce L_3 edge for the 5Fe5Ce and 10Ce catalysts. Two standards were also run, CeO_2 and $Ce(NO_3)_3.H_2O$, to show Ce^{4+} and Ce^{3+} states, respectively. The Ce spectra were collected from 83 eV below the edge to 416 eV above the edge to obtain a full spectrum, with a step size of 1.005113 eV. Linear combination fitting (LCF) was used as a semi-quantitative method to reveal the distribution of Ce^{3+} and Ce^{4+} in the 5Fe5Ce catalyst. The LCF fit, as flattened mu(E) from 5706.5 to 5806.5, included 117 data points, 3 variables and approximately 29.854 measurements.

2.3 Reactor setup

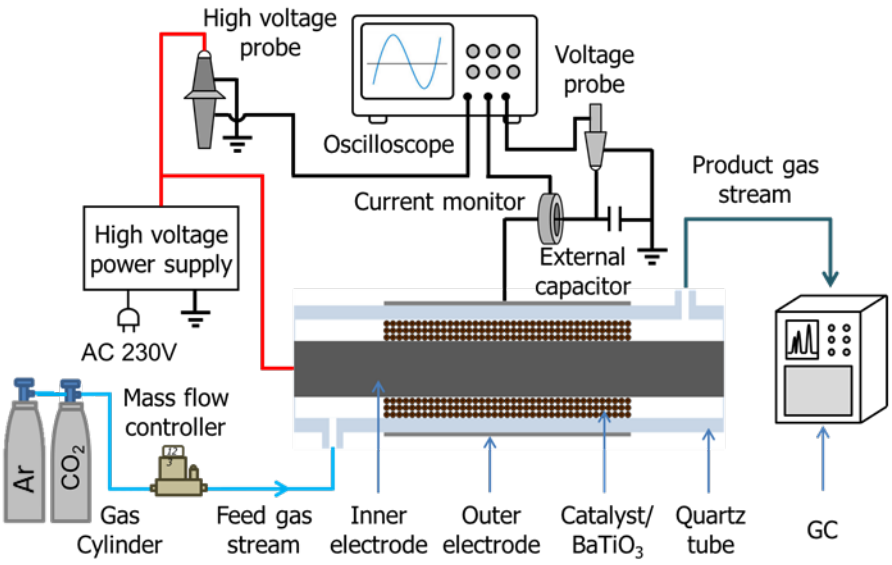

Figure 1. Schematic diagram of reactor setup for the CO_2 conversion

A coaxial dielectric barrier discharge plasma reactor (Figure 1), consisting of a quartz tube with inner diameter of 22 mm, was employed for these experiments. Wrapped around the quartz tube was a stainless-steel mesh forming the outer ground electrode, with a width of 60 mm, and placed inside the tube was the high voltage inner electrode; a stainless-steel rod of 16 mm diameter. The discharge gap was 3 mm, creating a discharge volume of 10.7 cm^3. The CO_2 inlet gas flow was kept constant throughout the experiment at 40 ml/min using a mass flow controller. For each experiment, 2 cm^3 (roughly 1.6 g) of catalyst (or pure gamma alumina beads) was mixed with 8 cm^3 packing material consisting of 1 mm $BaTiO_3$ beads (1:4 catalyst/$BaTiO_3$ volume ratio), before being placed in the reactor to give a packed bed configuration with quasi-homogeneous catalyst dispersion. The catalyst and packing material were held in the discharge gap by quartz wool placed either end of the discharge region. An AC high voltage power supply was used with a frequency of 9 kHz. All electrical signals were sampled by a 4-channel digital oscilloscope (TDS2014). The

discharge power was determined using the Q-U Lissajous figure and was controlled and monitored via a homemade online power measurement system in real time.[35–37] The discharge power was kept constant at 15 W throughout these experiments. Note that there were no obvious changes to the electrical signals of the discharge using different catalysts or γ-Al_2O_3. The gas temperature and the temperature of the catalyst bed were measured by an optical temperature fibre (Omega FOB102) inserted into the DBD reactor through a hole on the wall of the quartz tube. The temperature in the plasma gas phase was almost the same as that of the catalyst bed in the fully packed-bed DBD reactor. In addition, the presence of the catalysts in the DBD has limited effect on both temperatures, which were almost constant (120-130 ^{o}C) for different catalysts and γ-Al_2O_3 support.

Samples of the exit gas were taken before and during plasma discharge to enable the calculation of the reaction conversion (equation 2), as well as the energy efficiency (equation 3). A gas chromatograph (Shimadzu GC2014), equipped with dual detectors (thermal conductivity detector and flame ionization detector), was used to measure the components in the exit gas flow. When the reaction system reached a steady state after around 20 minutes, the gas products were analyzed by the gas chromatograph three times. The experiments were run for 2 hours and only minor fluctuations in CO_2 conversion and CO and O_2 yields were observed. The formation of ozone was monitored using an ozone detector (2B, Model106-M). However, ozone was not detected in this study.

The CO_2 conversion was calculated according to:

$$X_{CO_2}\ (\%) = \frac{CO_2\ converted\ (mol/s)}{CO_2\ input\ (mol/s)} \times 100 \qquad (2)$$

The energy efficiency was calculated according to:

$$\eta\ (\%) = \frac{CO_2\ flow\ rate\ (mol/s) \times X_{CO2}(\%) \times \Delta H(kJ/mol)}{Discharge\ power\ (kW)} \quad (3)$$

2.4 Plasma treatment of catalysts

Argon was used to better understand the influence of plasma on the reduction characteristics and structure variation (e.g., the formation of oxygen vacancy) of the 10Fe, 5Fe5Ce and 10Ce catalysts in the plasma conversion of CO_2. The reduction characteristics were explored using argon plasma as argon is stable and will not take part in any reaction. The aim of this experimental work using argon was to determine if the catalyst can be modified by the plasma, without any reaction taking place. These experiments were performed in the same DBD reactor using 20 W discharge power and 40 ml/min. Argon plasma treated catalysts were treated in pure Ar DBD for 2 hours, whilst the Ar/CO_2 plasma treated catalysts were first treated in pure Ar DBD for 2 hours followed by pure CO_2 DBD for 2 hours.

3. Results

3.1 Effect of Fe/Ce ratio on the catalyst structure and reaction performance

Table 1. BET analysis data, CO_2 conversion and energy efficiency of γ-Al_2O_3 and catalysts prepared with different Fe/Ce ratios.

Catalyst	BET surface area (m^2/g)	Pore volume (cm^3/g)	CO_2 conversion (%)	Energy efficiency (%)
γ-Al_2O_3	298	0.42	18.3	10.2
10Fe	192	0.44	13.3	7.4
7Fe3Ce	226	0.41	12.1	6.7
5Fe5Ce	209	0.44	24.5	13.6
3Fe7Ce	237	0.43	9.5	5.3
10Ce	195	0.40	28.2	15.7

The BET analysis results can be seen in Table 1. The supported iron oxide and ceria catalysts have a surface area close to 200 m^2/g. This is a significant decrease from the surface area of γ-Al_2O_3, showing the metal oxides blocked the pores of γ-Al_2O_3. γ-Al2O3 is known to be highly porous, with a large surface area, so coating the alumina bead with catalyst material that is of lower porosity decreases the surface area of the catalyst+alumina in comparison to alumina only. The surface area of the binary oxide catalysts increased slightly in comparison to their pure metal oxide counterparts, showing interactions between the two metal species[38,39]. The 5Fe5Ce catalyst has the smallest BET surface area of all the binary oxide catalysts, which may be due to substitution of Ce^{4+} by Fe^{3+}, as this leads to cubic CeO_2 undergoing lattice contraction[40]. This has been further explored using XRD analysis.

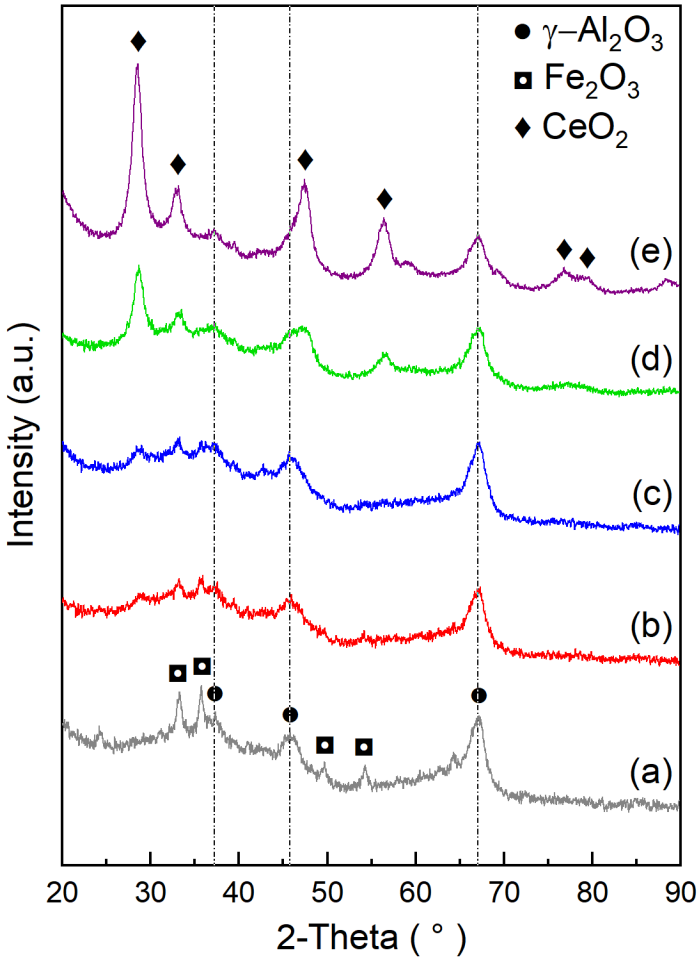

Figure 2. XRD patterns of (a) 10Fe; (b) 7Fe3Ce; (c) 5Fe5Ce; (d) 3Fe7Ce; (e) 10Ce.

The XRD patterns of calcined samples can be seen in Figure 2. The peak at 67.0° in all profiles is typical of γ-Al_2O_3 crystalline (JCPDS 00-010-0425). The Fe_2O_3 peaks in 10Fe (Figure 2 (a)) correspond to α-Fe_2O_3 (characteristic peaks at 2θ = 33°, 36°, 49° and 54°) with typical rhombohedra structure (JCPDS 80-2377). The addition of increasing amounts of cerium oxide into the iron oxide catalysts ((b)-(d)) caused a gradual enhancement in peak intensity of CeO_2 characteristic peaks at 28°, 33°, 47°, and 56°, corresponding to (111), (200), (220), and (311)

247 planes. Fe_2O_3 peaks in 7Fe3Ce (b) and 5Fe5Ce (c) are difficult to identify and the (104) Fe_2O_3
248 peak at 2θ = 33° is no longer prominent, revealing a change in orientation in comparison to the
249 10Fe catalyst. Peak intensity of the 5Fe5Ce catalyst (c) is at its lowest; hence this catalyst formed
250 a solid solution to the greatest extent.[38,40] As the ceria content was further increased in the 3Fe7Ce
251 catalyst (d), Fe_2O_3 peaks can no longer be seen due to one of three reasons: the concentration was
252 too low to detect by XRD; it is a highly amorphous phase; or a solid solution with cubic CeO_2
253 structure forms from Fe_2O_3 and CeO_2[40,41] CeO_2 peaks of the pure ceria catalyst (e) show it has the
254 typical fluorite structure (JCPDS 34-394).

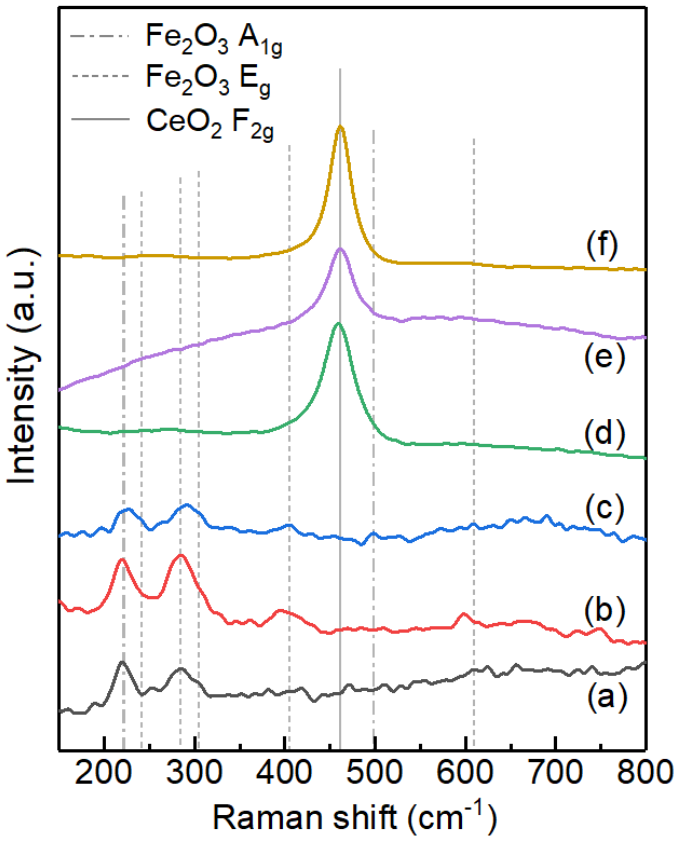

255

256 Figure 3. Raman shift spectra for (a) 10Fe; (b) 7Fe3Ce; (c) 5Fe5Ce; (d) 3Fe7Ce; and (e) 10Ce
257 catalysts

The Raman shift spectra (Figure 3) support the formation of a solid solution in the 7Fe3Ce and 5Fe5Ce catalysts as the characteristic band for CeO_2 at 465 cm^{-1} (from the F_{2g} mode) cannot be seen (Figures 3b and 3c);[42] only the bands for Fe_2O_3 due to A_{1g} (225 and 498 cm^{-1}) and E_g modes (247, 293, 299, 412, 613 cm^{-1}) are visible [43]. At the same ceria content as 5Fe5Ce, but without any iron oxide (5Ce), the CeO_2 band at 465 cm^{-1} can be seen clearly; thus a solid solution must have formed in the 5Fe5Ce catalyst. The band at 463 cm^{-1} occurs due to the symmetric breathing mode of oxygen atoms surrounding each Ce^{4+}.[40] A reduction in crystalline size of cubic CeO_2 can result in Raman features being absent; furthermore, hematite has a much stronger absorbance of the laser.[40] This supports the formation of a solid solution in the 5Fe5Ce catalyst as the interactions between Fe and Ce oxides result in changes to cubic CeO_2. As the ceria content was increased, from 7Fe3Ce to 5Fe5Ce, the iron oxide peaks became less sharp which reveals a decrease in crystallinity.[43] In the 3Fe7Ce catalyst only the characteristic peak for CeO_2 at 465 cm^{-1} can be seen, thus either the Fe_2O_3 content is too low to be detected or a solid solution has formed with CeO_2 structure.

The CO_2 conversion and energy efficiency, calculated according to equations 2 and 3, are shown in Table 1. The weight ratio of Fe/Ce had a profound effect on the CO_2 conversion. The 10Fe catalyst resulted in a low CO_2 conversion at 13.3%. The introduction of cerium into the 7Fe3Ce catalyst resulted in a slight decrease in CO_2 conversion in comparison to the 10Fe catalyst, to 12.1%; however, a further increase in Ce content (5Fe5Ce) led to a significantly higher CO_2 conversion at 24.5%. The 3Fe7Ce catalyst resulted in the lowest CO_2 conversion (9.5%). The 10Ce catalyst achieved the highest conversion, at 28.2%. The plasma-catalytic dissociation of CO_2 has a selectivity of almost 100% in both the presence and absence of a catalyst as no other carbon-

based products were formed. The formation of carbonates and carbon were not detected by Raman post-reaction. As can be seen from Table 1, the energy efficiency (calculated using equation 3) follows the same pattern as the CO_2 conversion: 10Ce > 5Fe5Ce > γ-Al_2O_3 > 10Fe > 7Fe3Ce > 3Fe7Ce. This result therefore shows that there is an optimum Fe/Ce ratio for the CO_2 decomposition reaction, at which the interaction between the two metals is highly beneficial on the reaction performance. The 5Fe5Ce catalyst can be considered the optimum, as the CO_2 conversion was comparable to that of pure ceria whilst the use of a costly, rare earth metal has been greatly reduced.

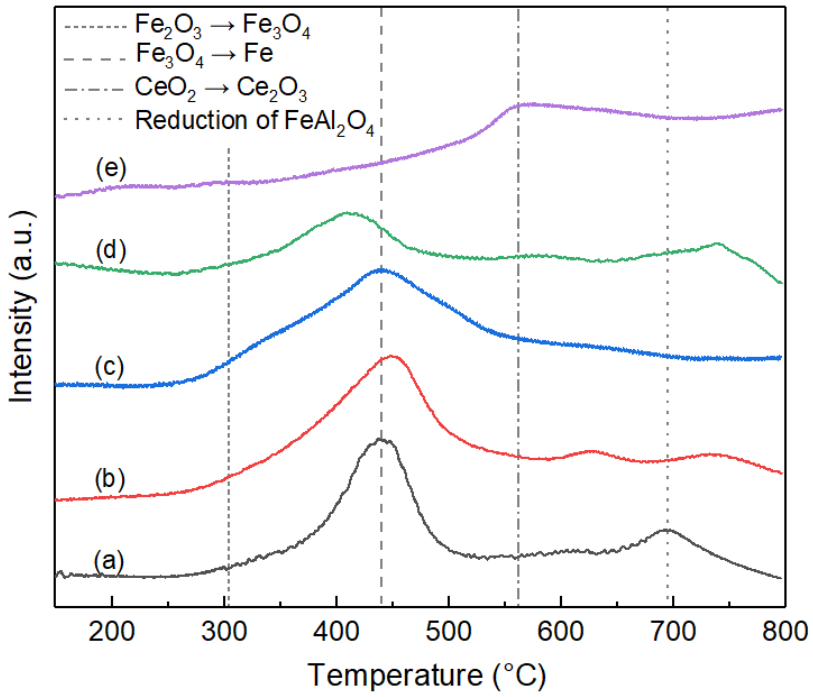

Figure 4. H_2-TPR spectra for (a) 10Fe; (b) 7Fe3Ce; (c) 5Fe5Ce; (d) 3Fe7Ce; (e) 10Ce catalysts.

In order to elucidate any link between catalyst reducibility and CO_2 conversion, H_2-temperature programmed reduction was carried out.

$$Fe_2O_3(s) \rightarrow Fe_3O_4(s) \rightarrow Fe(s) \quad (4)$$

$$CeO_2(s) \rightarrow Ce_2O_3(s) \quad (5)$$

From Figure 4 (a), it can be seen that 10Fe underwent reduction at low temperature (260-510 °C) via the pathway given in equation 4. The first reduction at 340 °C is attributed to reduction of Fe_2O_3 to Fe_3O_4, whilst Fe_3O_4 is reduced to Fe at 440 °C. The high temperature reduction peak at 700 °C is attributed to strong interactions between iron and the alumina support,[44,45] most probably the reduction of iron aluminate. With regards to 7Fe3Ce (Figure 4 (b)), the addition of 3 wt.% Ce increased the intensity of the low temperature iron oxide reduction peak at 340 °C but shifted the peak for Fe_3O_4 reduction to a slightly higher temperature (450 °C). Two peaks at 640 °C and 740 °C can be seen which may be due to catalyst-support interactions requiring higher temperatures to reduce aluminate species. Increasing the CeO_2 content further to 5 wt.% (c), resulted in the reduction of iron oxide occurring over a larger temperature range for 5Fe5Ce (260-540 °C). This is most likely due to the CeO_2 peak shifting and merging with the iron oxide peak; hence CeO_2 was reduced at a lower temperature due to the promotional effect of Fe, which activates H_2 and spills over to CeO_2. The Fe_3O_4 reduction peak for the 5Fe5Ce catalyst occurs at the same temperature as that of 10Fe (440 °C). At the addition of more CeO_2, the Fe_3O_4 reduction peak of the 3Fe7Ce catalyst (d) shifts to a lower temperature (420 °C), but is much less intense. A peak for CeO_2 reduction via equation 5 can again be seen at around 575 °C, along with another peak at 740 °C, which is attributable to catalyst-support interactions. The reduction of the pure ceria catalyst, 10Ce, occurred at high temperature, roughly 525-700 °C (e). This reduction occurs due

to removal of oxygen from the surface of ceria via equation 5.[41] Further reduction of ceria can occur as oxygen is removed from the bulk of the catalyst; however, this cannot be seen in (e), as the temperature was too low (<800 °C).[41] This finding clearly shows that the lowest reduction temperature was achieved on 5Fe5Ce, consistent with the highest CO_2 conversion achieved (24.5%) of all the ceria-doped iron catalysts. However, 10Ce still showed the best performance, (with a CO_2 conversion of 28.2%), without showing the low temperature reduction peak at 340 °C; thus, other factors must influence the activity of ceria in this reaction.

The difference in reduction temperatures of the catalysts under H_2 flow from 30 to 800 ^oC has been shown; however, in the CO_2 DBD plasma, the gas temperature was less than 150 ^oC and as no hydrogen was present, reduction occurred via catalyst interaction with plasma generated species (i.e. highly energetic electron bombardment of the catalyst surface). In order to gain new insights into the reduction characteristics and the structure variation of the catalysts in plasma, Ar DBD and Ar/CO_2 DBD plasma treatment of 10Fe, 5Fe5Ce and 10Ce catalysts were carried out and XPS analysis of the catalysts before and after the plasma treatment was performed.

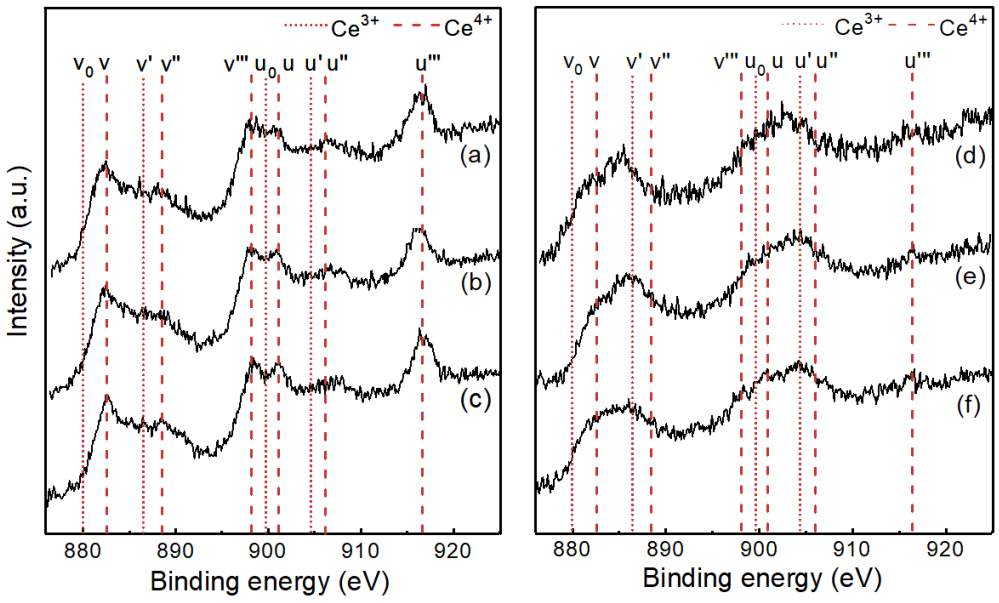

Figure 5. Ce 3d XPS spectra of 10Ce (a) before plasma treatment; (b) Ar plasma treated; (c) Ar/CO_2 plasma treated; and 5Fe5Ce (d) before plasma treatment; (e) Ar plasma treated; (f) Ar/CO_2 plasma treated catalysts; with labelled v & u doublets: dotted lines are attributed to Ce^{3+} peaks, dashed lines to Ce^{4+}.

The Ce 3d XPS spectra of the fresh (before plasma treatment), Ar plasma treated and $Ar+CO_2$ plasma treated catalysts can be seen in Figure 5. Two multiplets can be identified in Ce3d XPS spectra: u and v. These correspond to Ce $3d_{3/2}$ and Ce $3d_{5/2}$ spin-orbit split core holes, respectively, within which 3 doublets can be identified which are divided into 6 peaks overall. In Ce 3d spectra, u''' is attributed to Ce^{4+} ions in the Ce 3d3/2 spin orbit and this, along with v''', results from a final Ce state of $3d^9\ 4f^0\ O\ 2p^6$.[46] They have the highest binding energy for each spin-orbit split. Conversely, the lower binding energy states (u, v, u'', v''), result from Ce final states of 3d9 4f2 O 2p4 and 3d9 4f1 O 2p5.[46] In Figure 5, the doublets corresponding to Ce^{4+} are v and u, v'' and u'', and v''' and u''', located at 882.0, 900.6, 888.0, 906.6, 898.0 and 916.6 eV binding energies, respectively. Doublets corresponding to Ce^{3+} are labelled v_0 and u_0, and v' and u' and are located at 880.0, 898.6, 886.0 and 904.6 eV binding energies, respectively.

Comparing Ce 3d spectra (Figure 5) of 10Ce ((a)-(c)) and 5Fe5Ce ((d)-(f)), it is obvious that changes in ceria have occurred due to the combination of the two metal oxides. The fresh 10Ce and 5Fe5Ce catalysts XPS spectra ((a) and (c), respectively) have different relative peak intensities. The 10Ce spectrum (a) has intense Ce^{4+} peaks, (v & u, v'' & u'' and v''' & u'''), whilst peaks for Ce^{3+} are of much lower intensity. On the other hand, the opposite is true for 5Fe5Ce (c); Ce^{3+} peaks (v_0 & u_0 and v' & u') are more intense than Ce^{4+} peaks. The peaks for v & u can still

clearly be seen; however, v'' & u'' and v''' & u''' peaks are of very low intensity. The relative intensity of the u''' peak in comparison to the total intensity of all peaks reveals the degree of reduction. The fresh 5Fe5Ce catalyst therefore contains a higher concentration of Ce^{3+} than fresh 10Ce.

Very little change can be seen after argon plasma treatment of both 10Ce (b) and 5Fe5Ce (e). After argon and CO_2 plasma treatment, again no change can be seen in the peak intensities of the 10Ce catalyst; however, in the 5Fe5Ce spectrum (f), it can be seen that the relative intensity of Ce^{4+} to Ce^{3+} has increased. The 5Fe5Ce catalyst was therefore partially oxidized in CO_2 plasma.

Fresh 10Ce and 5Fe5Ce catalysts were also analyzed using XANES to further characterize their electronic properties (Figure 6). Standard commercial CeO_2 powder (Strem Chemicals) and $Ce(NO_3)_3 \cdot 6H_2O$ (Alfa Aesar) were used as references to show the Ce^{4+} and Ce^{3+} states, respectively. For the former, two peaks can be seen at around 5733 and 5740 eV due to Ce^{4+}; these are commonly referred to as B1 and C, respectively.[47] The $Ce(NO_3)_3.6H_2O$ sample shows only one peak at lower energy (5727 eV) due to Ce^{3+}.

It can be seen from Figure 6 that the XANES spectrum at the Ce L_3 edge of the 10Ce catalyst is very similar in shape to the CeO_2 standard powder as it contains two peaks, the second of which is less intense than the first. Cerium in this catalyst was therefore present in the Ce^{4+} state.

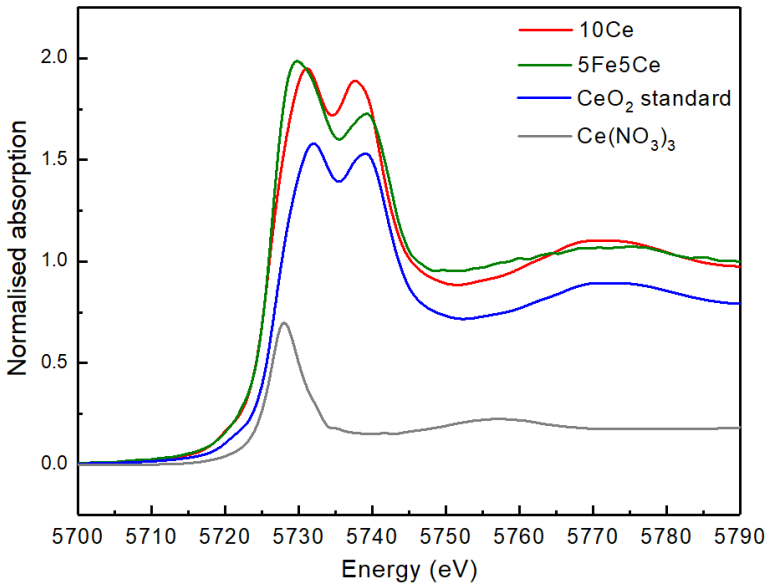

369

370 Figure 6. XANES spectra of Ce L_3 edge for the fresh 10Ce and 5Fe5Ce catalysts along with CeO_2

371 and $Ce(NO_3)_3$ standards to show Ce^{4+} and Ce^{3+} spectra, respectively.

372

373 The 5e5Ce catalyst XANES spectrum also contains two peaks at the Ce L_3 edge; however, a shift

374 to lower photon energy has occurred in comparison to the 10Ce catalyst and the intensity of the

375 first peak in comparison to the second peak is much larger. Linear combination fitting has been

376 used to calculate the percentage of Ce^{3+} in the 5Fe5Ce catalyst and thus the degree of reduction.

377 The concentration of Ce^{3+} and Ce^{4+} was 19% and 81%, respectively, determined by the LCF fitting.

378 This result supports the XPS data, which showed 5Fe5Ce to be more electron-rich than 10Ce.

379

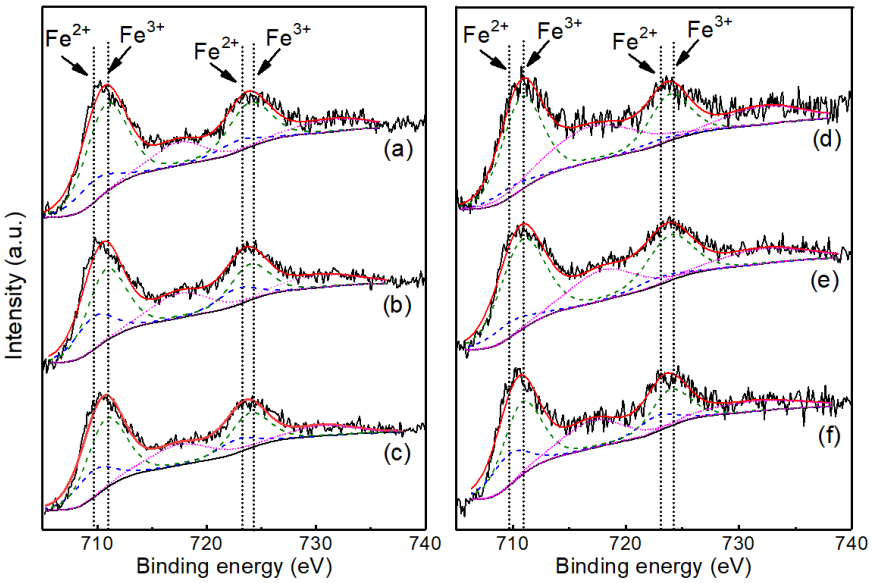

Figure 7. Fe 2p XPS spectra of 10Fe (a) before plasma treatment; (b) Ar plasma treated; (c) Ar/CO_2 plasma treated; and 5Fe5Ce (d) before plasma treatment; (e) Ar plasma treated; (f) Ar/CO_2 plasma treated.

With regards to the fresh 10Fe (Figure 7 (a)) and fresh 5Fe5Ce (Figure 7 (d)) catalysts, two Fe^{2+} peaks can be seen in the XPS spectra at 709.6 eV (Fe $2p_{3/2}$) and 722.7 eV (Fe $2p_{1/2}$). Two peaks can also be seen at 710.8 eV (Fe $2p_{3/2}$) and 723.9 eV (Fe $2p_{1/2}$), which are attributed to Fe^{3+}. The two other peaks are satellite peaks. The composition of the iron oxide phase was calculated by the comparison of the peak areas.[48] As can be deduced from Figure 7, Fe^{2+} peaks become more intense and Fe^{3+} less intense after Ar plasma treatment of the catalysts. After Ar/CO_2 plasma treatment of 10Fe, Fe^{2+} peak area decreases, whilst for 5Fe5Ce the opposite occurs.

In summary, the addition of cerium into Fe_2O_3 can improve the CO_2 conversion and energy efficiency up to a point; above 5 wt.% CeO_2 the reaction performance declined. The performance of the Ce-promoted catalysts is related to the formation of a solid solution and the reducibility of the catalyst, as evidenced by H_2-TPR, XRD and XPS and XANES. In order to further explore how

395 catalyst preparation method can affect catalytic performance, the optimum bimetallic catalyst
396 (5Fe5Ce) was selected to carry out a study on metal loading sequence during catalyst synthesis.

397

398 **3.2 Effect of synthesis method**

399 As these catalysts have almost identical surface area, pore size and composition (Table 2), the
400 effect of these catalysts on the discharge characteristics is also very limited, thus the difference in
401 CO_2 conversion should be attributed to structure.

402 **Table 2.** BET surface analysis data, CO_2 conversion and energy efficiency of 5Fe5Ce catalysts
403 prepared using co-impregnation and sequential loading orders of the metal species

Catalyst	BET surface area (m^2/g)	Pore volume (cm^3/g)	CO_2 conversion (%)	Energy efficiency (%)
5Fe5Ce	209	0.437	24.5	13.6
5Fe5Ce(Fe)	199	0.418	10.1	5.6
5Fe5Ce(Ce)	209	0.419	13.3	7.4

404

405

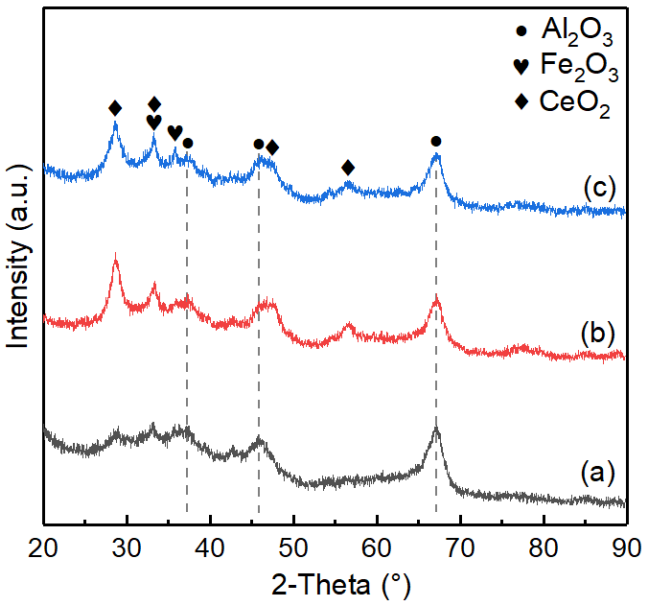

406

407 Figure 8. XRD patterns of (a) 5Fe5Ce; (b) 5Fe5Ce (Fe); (c) 5Fe5Ce (Ce)

408

409 The XRD results of the three catalysts revealed a decrease in peak intensity for the co-loaded
410 catalyst (Figure 8 (a)) in comparison to the sequentially loaded catalysts (Figure 8 (b) & (c)). This
411 decrease in intensity could be due to the formation of a solid solution, as this would interfere with
412 the diffraction patterns of the pure metal oxides. The high CO_2 conversion attained using the co-
413 loaded catalyst (24.5%) is attributed to the solid solution formation and the effect this has on the
414 catalyst properties. In the case of the sequentially loaded catalysts 5Fe5Ce(Fe) and 5Fe5Ce(Ce),
415 much clearer peaks of CeO_2 can be seen in the XRD patterns (Figures 8 (b) & (c), respectively),
416 suggesting that the extent of interactions between the two metal oxides is lower via this type of
417 synthesis and that the phases mostly remain separate. The XRD pattern of sequentially loaded
418 5Fe5Ce(Ce) has a more pronounced characteristic Fe_2O_3 peak at 36°, which is barely visible for
419 5Fe5Ce(Fe). This again indicates greater interaction between iron and the support when iron is
420 loaded onto the support first. The difference in reaction performance between the sequentially

loaded catalysts may therefore be due to the formation of an aluminate occurring more readily between iron and alumina when iron is loaded first than between cerium and alumina when cerium is loaded first; thus, reducing the formation of a solid solution and leading to a decrease in CO_2 conversion for the 5Fe5Ce(Fe) catalyst (10.1%), in comparison to the 5Fe5Ce(Ce) catalyst (13.3%).

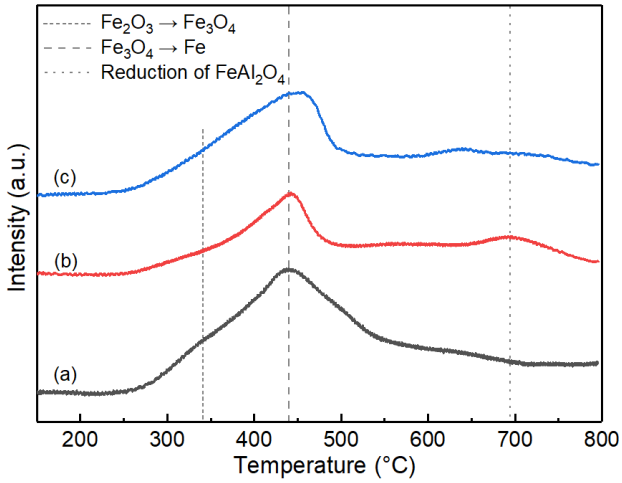

Figure 9. H_2-TPR data for (a) 5Fe5Ce, (b) 5Fe5Ce(Fe) and (c) 5Fe5Ce(Ce).

The metal loading order of the 5Fe5Ce catalyst clearly affected the catalyst reducibility, as shown by the H_2-TPR data, Figure 9. Although all three catalysts began reducing at roughly the same temperature, the co-impregnated catalyst (Figure 9 (a)) reduced over the widest temperature range (260-540 °C) and the initial reduction of iron oxide via equation 4 (Fe_2O_3 → Fe_3O_4) occurred at low temperature (340 °C). The 5Fe5Ce(Fe) catalyst underwent a high temperature reduction at roughly 700 °C (Figure 9 (b)). This corresponds to reduction of iron aluminate ($FeAl_2O_4$) due to strong catalyst-support interactions when Fe is loaded onto the support first.[44] A very low intensity

reduction peak can be seen for 5Fe5Ce(Ce) at 640 °C (c), which corresponds to the reduction of ceria (equation 5). The high temperature iron aluminate reduction peak is not visible and iron oxide reduction occurred between 260 and 500 °C for 5Fe5Ce(Ce).

4. Discussions

4.1 The role of catalyst oxygen vacancy sites to enhance CO_2 conversion in plasma

In plasma-catalysis, both homogenous and heterogeneous reactions can occur. Homogeneous reactions occur in the plasma gas phase, as electrons generated in the plasma collide with a CO_2 molecule and dissociate it via electron impact dissociation (equation 6), which has been regarded as a dominant reaction for CO_2 conversion in a DBD reactor. In addition, electron dissociative attachment (equation 7) and electron impact ionization (equation 8) also exist in the plasma processing of CO_2.

$$e^- + CO_2(g) \rightarrow CO(g) + O(g) + e^- \quad (6)$$

$$e^- + CO_2(g) \rightarrow CO(g) + O^-(g) \quad (7)$$

$$e^- + CO_2(g) \rightarrow {CO_2}^+(g) + 2e^- \quad (8)$$

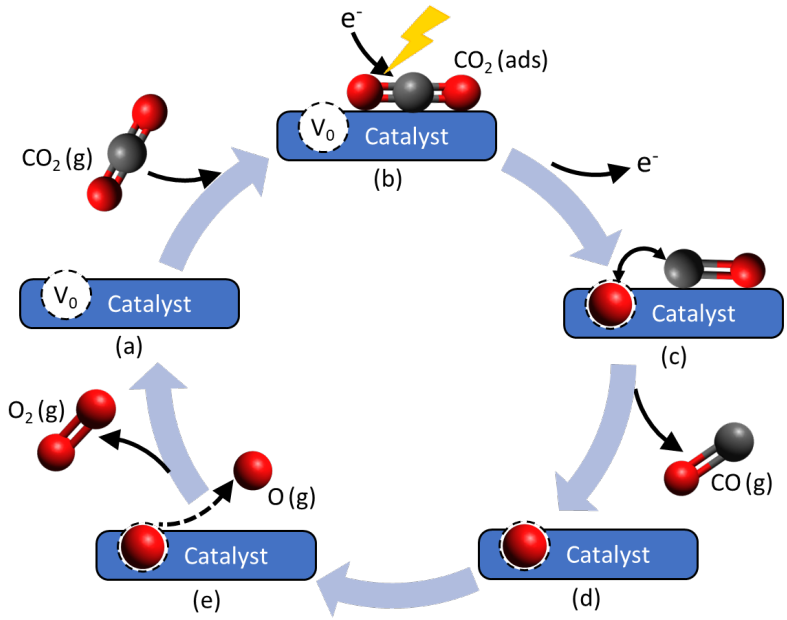

450

451 Figure 10. CO_2 dissociation mechanism via dissociative electron attachment at the catalyst

452 surface

453

454 Alongside these gas phase reactions, CO_2 can be dissociated at the catalyst surface. In this work,

455 CO_2 decomposition was carried out in a fully packed-bed DBD reactor. There were no obvious

456 changes to the electrical signals of the discharge when using different metal oxide catalysts and γ-

457 Al_2O_3 support, indicating that the presence of these metal oxides does not change the discharge

458 properties significantly. Moreover, the temperature of the catalyst bed was almost constant for

459 different catalysts and γ-Al_2O_3 support. These findings suggest that the difference in the CO_2

460 conversion for different catalysts can be largely dependent on the characteristics of the catalysts

461 and associated surface reactions. Figure 10 depicts the proposed reaction mechanism based on the

462 analysis of CO_2 decomposition over the Fe/Ce binary oxides using different Fe/Ce ratios and

463 loading orders through a comprehensive characterization of fresh, Ar DBD and Ar/CO_2 DBD

treated catalysts. It is thought that the CO_2 molecule dissociates at oxygen vacancy sites on the catalyst surface, as reported in previous work when using TiO_2 and $BaTiO_3$ catalysts.[8] Under plasma, catalysts could be reduced as oxygen is removed from the crystal according to Figure 10 (a). The highly energetic electrons generated in the plasma could facilitate this process. Once a CO_2 molecule is adsorbed on the catalyst surface, the double bond is broken as electrons generated in the plasma collide with the molecule (Figure 10 (b)). The process results in the formation of CO and O^- ion via production of the transient CO_2^- ion.[49] The CO_2^- ion is known to easily form in the presence of ceria as CO_2 is commonly used to probe the basicity of CeO_2.[50] It has also been shown that CO_2^- can form in a similar manner during plasma CO_2 decomposition over TiO_2.[8,49] The CO molecule then desorbs from the catalyst surface and the oxygen ion loses an electron to form an oxygen atom that fills the vacancy site on the catalyst surface. An oxygen atom present in the plasma can then recombine with the oxygen atom at the catalyst surface, forming an O_2 molecule that desorbs from the surface to reform the oxygen vacancy site.

The H_2-TPR results (Figure 4) revealed the 10Fe catalyst had a low reduction temperature whilst XPS (Figure 7) again showed the catalyst was reduced and re-oxidized in plasma. However, the CO_2 conversion of 10Fe was even lower than the bare γ-Al_2O_3 beads, probably due to 10Fe catalysing the reverse CO_2 decomposition reaction (equation 9).

$$3Fe_2O_3(s) + CO(g) \rightarrow 2Fe_3O_4(s) + CO_2(g) \quad (9)$$

Addition of a suitable amount of Ce (5Fe5Ce) into the iron oxide catalyst significantly enhanced the activity of Fe_2O_3 for the CO_2 conversion in plasma, almost doubling the CO_2 conversion in comparison to the 10Fe catalyst (Table 1). This was due to the formation of a solid solution with enhanced redox properties and number of oxygen vacancies, as well as the presence of Ce^{3+} in the

catalyst before the reaction (as evidenced by XANES, Figure 6). XPS showed a greater concentration of Fe^{2+} after Ar and after Ar+CO_2 plasma treatment, suggesting that the iron oxide species was reduced in-situ by plasma species. As this catalyst had half the iron content of the 10Fe catalyst, reduction of iron oxide via equation 9 would have been dampened. A lower concentration of Ce^{3+} was found to be present after Ar/CO_2 plasma treatment, revealing the ceria species was re-oxidised and therefore supporting the proposed mechanism for CO_2 dissociation. As 5Fe5Ce contained Ce^{3+} before the reaction, it is reasonable that this catalyst will appear more oxidised after the reaction as reduction and oxidation reactions will be occurring continuously.

4.2 The role of Ce doping to enhance oxygen vacancies

A comparison of the Fe/Ce catalysts prepared using different ratios showed the CO_2 conversion achieved followed the same order as the extent to which a solid solution was formed (as evidenced by XRD, Figure 2), decreasing in the order: 5Fe5Ce > 7Fe3Ce > 3Fe7Ce, (24.5%, 12.1 % and 9.5%, respectively). This trend was also mirrored in the reducibility of the catalysts during H_2-TPR (Figure 4). The 5Fe5Ce catalyst had the largest $Fe_2O_3 \rightarrow Fe_3O_4$ reduction peak and started reducing at the lowest temperature (260 °C), followed by 7Fe3Ce. The H_2-TPR data also did not show any high temperature reduction peaks for 5Fe5Ce, attributable to reduction of iron-aluminates, which were present for 7Fe3Ce and 3Fe7Ce; thus 5Fe5Ce can be reduced to a greater extent at low temperature as catalyst-support interactions are weaker. In the CO_2 plasma, the bulk gas temperature was between 250 and 300 °C; hence 5Fe5Ce could be further reduced than 7Fe3Ce and 3Fe7Ce, leading to the formation of a greater number of oxygen vacancies available to facilitate CO_2 dissociation.

When combining iron and cerium oxides, a solid solution can form with an increased number of oxygen vacancy sites. This appears to be the case for the 5Fe5Ce catalyst, as the XRD spectrum contains only very low intensity α-Fe_2O_3 and CeO_2 peaks (Figure 2 (c)) and the Raman spectrum only shows peaks for Fe_2O_3 (Figure 3 (b)), an indication that the crystalline size of CeO_2 has reduced due to the substitution of Ce^{4+} with Fe^{3+}, as explained in section 3.1 Effect of Fe/Ce ratio on the catalyst structure and reaction performance.[40] The H_2-TPR data also showed this catalyst could be reduced at low temperatures (Figure 4 (c)) whilst the XANES study revealed the presence of Ce^{3+} (Figure 6). In 7Fe3Ce the concentration of ceria was too low to enhance the number of oxygen vacancies, as a solid solution could not form to such a great extent (evidenced by the increase in XRD peak intensity Figure 2 (b)).

The number of oxygen vacancies in the mixed oxide catalysts is dependent on the substitution of Ce^{4+} by Fe^{3+}. At low iron concentrations, two Fe^{3+} take the place of two Ce^{4+}, creating one oxygen vacancy to balance the charge.[40] The number of oxygen vacancies rises with the iron content, up to a critical concentration of iron. This critical iron content must be close to that in the 5Fe5Ce catalyst as this had the highest CO_2 conversion. At low iron concentrations, such as for the 3Fe7Ce catalyst, the lower iron content resulted in a decrease in the number of oxygen vacancies in comparison to 5Fe5Ce; hence this catalyst had a low CO_2 conversion. At higher iron concentrations, above the critical point, the doping mechanism changes as three Fe^{3+} take the place of three Ce^{4+} and an additional Fe^{3+} takes up residence in the cubic CeO_2 interstitial sites.[40] This is accompanied by a reduction in oxygen vacancies. This can therefore account for the low CO_2 conversion achieved over the 7Fe3Ce catalyst.

4.3 The role of synthesis method in maximising solid solution formation

The order in which Fe and Ce were loaded onto the alumina support was found to affect reaction performance due to the influence this had on the formation of a solid solution. The co-loaded 5Fe5Ce catalyst achieved the highest conversion at 24.5 %, followed by the 5Fe5Ce(Ce) catalyst (13.3%) and finally the 5Fe5Ce(Fe) catalyst (10.1%). As stated previously, the extent to which a solid solution formed determined the number of oxygen vacancy sites in the catalyst and thus the CO_2 conversion as CO_2 dissociation occurred at these vacancy sites in the mixed oxide catalysts. The XRD results showed a solid solution formed to the greatest extent in the co-loaded catalyst, as peak intensities were much lower than in the 5Ce5Ce(Fe) and 5Ce5Ce(Ce) catalyst spectra. Both 5Fe5Ce(Ce) and 5Fe5Ce(Fe) showed a decrease in reducibility at low temperature (Figure 9) and in CO_2 conversion in plasma (Table 2) in comparison to co-loaded 5Fe5Ce (Figure 9) due to this.

The difference in CO_2 conversion between the ceria loaded first and iron loaded first catalysts can be attributed to the varying degree of interaction between each metal and the alumina support. A high temperature reduction peak was present in the 5Fe5Ce(Fe) H_2-TPR data (Figure 9 (b)). This peak is attributable to iron species which have a strong interaction with γ-Al_2O_3. This interaction with the support is detrimental to the reaction performance as it results in a smaller concentration of Fe_2O_3 that can form a solid solution and hence undergo low temperature reduction to facilitate CO_2 decomposition. Cerium does not interact as strongly with the support; high temperature reduction peaks cannot be seen in the H_2-TPR spectra of 5Fe5Ce(Ce). The 5Fe5Ce(Ce) catalyst therefore has a greater concentration of iron that can interact with cerium and form a solid solution, increasing the extent of reduction at low temperature above that of 5Fe5Ce(Fe).

5. Conclusion

The conversion of CO_2 to CO and O_2 has been investigated over iron oxide, ceria and ceria-promoted iron oxide catalysts with various Fe/Ce ratios in a non-thermal DBD plasma reactor at low temperatures and atmospheric pressure. It was found that the extent to which a solid solution forms in the Fe/Ce bimetallic oxide catalysts has a direct correlation to the reaction performance. This is because when a solid solution forms, the catalyst can be both reduced and form oxygen vacancies more facilely than when iron oxide and ceria remain in two distinct, separate phases. The formation of a greater number of oxygen vacancies increases the CO_2 conversion as oxygen vacancies are the active site for CO_2 dissociation. The optimum Fe/Ce catalyst was found to be the co-loaded 5Fe5Ce catalyst (24.5 % CO_2 conversion and 13.6% energy efficiency), as this formed a solid solution to the greatest extent as two Fe^{3+} substituted two Ce^{4+}, which was accompanied by the formation of an oxygen vacancy site. The 10Fe catalyst, although easily reducible, had a low CO_2 conversion, which could be associated with promotion of the reverse reaction to reform CO_2 by this catalyst. Overall, the highest conversion and energy efficiency were achieved over 10Ce; however, this was not linked to the formation of oxygen vacancies. Although the CO_2 conversion of the 10Ce catalyst was slightly higher than that of the 5Fe5Ce catalyst (28.2 and 24.5 %, respectively), the 5Fe5Ce catalyst contains far less ceria. As ceria is an expensive, rare-earth metal, the use of the 5Fe5Ce catalyst would significantly decrease operating costs whilst resulting in only a slight decrease in conversion. 5Fe5Ce catalyst would significantly decrease operating costs whilst resulting in only a slight decrease in conversion.

Acknowledgements

Support of this work by the Doctoral Training Program at the University of Liverpool, UK, and the A* STAR Research Attachment Program (ARAP), Singapore is gratefully acknowledged. This project has received funding from the European Union's Horizon 2020 research and innovation programme under the Marie Skłodowska-Curie grant agreement No 823745. The support of April Wang Zhan at the Institute of Chemical and Engineering Sciences, Singapore, in carrying out XPS analysis and that of Dr Du Yong Hua and Dr Xi Shi Bo for performing XANES analysis is also appreciatively accredited.

References

1 T. Oberreuther, C. Wolff and A. Behr, *IEEE Trans. Plasma Sci.*, 2003, **31**, 74–78.

2 Y. X. Zeng, L. Wang, C. F. Wu, J. Q. Wang, B. X. Shen and X. Tu, *Appl. Catal. B Environ.*, 2018, **224**, 469–478.

3 D. Li, V. Rohani, F. Fabry, A. Parakkulam Ramaswamy, M. Sennour and L. Fulcheri, *Appl. Catal. B Environ.*, 2020, **261**, 2–9.

4 S. Xu, S. Chansai, Y. Shao, S. Xu, Y. chi Wang, S. Haigh, Y. Mu, Y. Jiao, C. E. Stere, H. Chen, X. Fan and C. Hardacre, *Appl. Catal. B Environ.*, 2020, **268**, 118752.

5 G. Chen, T. Godfroid, N. Britun, V. Georgieva, M. P. Delplancke-Ogletree and R. Snyders, *Appl. Catal. B Environ.*, 2017, **214**, 114–125.

6 J. Wang, G. Xia, A. Huang, S. L. Suib, Y. Hayashi and H. Matsumoto, *J. Catal.*, 1999, **185**, 152–159.

7 L. F. Spencer and A. D. Gallimore, *Plasma Chem. Plasma Process.*, 2011, **31**, 79–89.

8 D. Mei, X. Zhu, C. Wu, B. Ashford, P. T. Williams and X. Tu, *Appl. Catal. B Environ.*, 2016, **182**, 525–532.

9 R. Aerts, W. Somers and A. Bogaerts, *ChemSusChem*, 2015, **8**, 702-716.

10 L. Wang, Y. Yi, H. Guo and X. Tu, *ACS Catal.*, 2018, **8**, 90–100.

11 H. J. Gallon, X. Tu and J. C. Whitehead, *Plasma Process. Polym.*, 2012, **9**, 90–97.

12 H. Chen, Y. Mu, Y. Shao, S. Chansai, S. Xu, C. E. Stere, H. Xiang, R. Zhang, Y. Jiao, C. Hardacre and X. Fan, *Catal. Sci. Technol.*, 2019, **9**, 4135–4145.

13 R. Snoeckx and A. Bogaerts, *Chem. Soc. Rev.*, 2017, **46**, 5805–5863.

14 C. E. Stere, J. A. Anderson, S. Chansai, J. J. Delgado, A. Goguet, W. G. Graham, S. F. R. Taylor, X. Tu, Z. Wang and H. Yang, *Angew. Chem Int. Ed. Commun.*, 2017, **56**, 5579–5583.

15 A. Bogaerts, T. Kozak, K. Van Laer and R. Snoeckx, *Faraday Discuss.*, 2015, **183**, 217–232.

16 X. Wang, L. Zhu, Y. Liu and S. Wang, *Sci. Total Environ.*, 2018, **625**, 686–695.

17 Q. Yu, M. Kong, T. Liu, J. Fei and X. Zheng, *Plasma Chem. Plasma Process.*, 2012, **32**, 153–163.

18 K. Zhang, G. Zhang, X. Liu, A. N. Phan and K. Luo, *Ind. Eng. Chem. Res.*, 2017, **56**, 3204–3216.

19 Q. Yu, M. Kong, T. Liu, J. Fei and X. Zheng, *Plasma Chem. Plasma Process.*, 2012, **32**, 153–163.

20 K. Van Laer and A. Bogaerts, *Energy Technol.*, 2015, **3**, 1038–1044.

21 G. Chen, N. Britun, T. Godfroid, V. Georgieva, R. Snyders and M. P. Delplancke-Ogletree, *J. Phys. D. Appl. Phys.*, 2017, **50**, 8.

22 L. F. Spencer, *Master Thesis*, 2012, 198.

23 M. V. Ganduglia-pirovano, *Catal. Today*, 2015, **253**, 20–32.

24 T. Staudt, Y. Lykhach, N. Tsud, T. Skála, K. C. Prince, V. Matolín and J. Libuda, *J. Catal.*, 2010, **275**, 181–185.

25 R. X. Valenzuela, G. Bueno, V. Cortés, Y. Xu and C. Chen, *Catal. Today*, 2000, **61**, 43–48.

26 N. P. Spiegel, S. Livers, J. E. Miller and R.B. Diver, *Proceed. ASME 2010 4th Int. Conference on Energy Sus.*, 2010, ES2010-90091.

27 W. Qi, K. Xie, Q. Qin, Q. Zhou, Y. Wang, Y. Zhang and Y. Wu, *J. Solid State Electrochem.*, 2014, **18**, 3415–3425.

28 N. V. Skorodumova, R. Ahuja, S. I. Simak, I. A. Abrikosov, B. Johansson and B. I. Lundqvist, *Phys. Rev. B*, 2001, **64**, 115108.

29 G. K. Pradhan and K. M. Parida, *Int. J. Eng. Sci. Technol.*, 2010, **2**, 53–65.

30 Y. Lykhach, T. Staudt, M. P. A. Lorenz, R. Streber, A. Bayer, H. P. Steinrück and J. Libuda, *ChemPhysChem*, 2010, **11**, 1496–1504.

31 S. S. Kim, S. M. Lee and S. C. Hong, *J. Ind. Eng. Chem.*, 2012, **18**, 860–864.

32 Z. Wang, Y. Zhang, E. C. Neyts, X. Cao, X. Zhang, B. W. Jang and C. Liu, *ACS Catal.*, 2018, **8**, 2093–2110.

33 A. S. Bobin, V. A. Sadykov, V. A. Rogov, N. V Mezentseva, G. M. Alikina, E. M. Sadovskaya, T. S. Glazneva, N. N. Sazonova, M. Y. Smirnova, S. A. Veniaminov, C. Mirodatos, V. Galvita and G. B. Marin, *Top. Catal.*, 2013, **56**, 958–968.

34 R. P. Ye, Q. Li, W. Gong, T. Wang, J. J. Razink, L. Lin, Y. Y. Qin, Z. Zhou, H. Adidharma, J. Tang, A. G. Russell, M. Fan and Y. G. Yao, *Appl. Catal. B Environ.*, 2020, **268**, 118474.

35 Y. Wang, M. Craven, X. Yu, J. Ding, P. Bryant, J. Huang and X. Tu, *ACS Catal.*, 2019, **9**, 10780–10793.

36 Y. X. Zeng, L. Wang, C. F. Wu, J. Q. Wang, B. X. Shen and X. Tu, *Appl. Catal. B Environ.*,

2018, **224**, 469–478.

37 D. Mei, X. Zhu, Y.-L. He, J. D. Yan and X. Tu, *Plasma Sources Sci. Technol.*, 2015, **24**, 15011–15021.

38 L. Liu, S. Wu, J. Chen, C. Zheng, X. Gao, M. Ni and K. CEN, *Chinese J. Catal.*

39 J. Wang, M. Shen, J. Wang, M. Cui, J. Gao, J. Ma and S. Liu, *J. Environ. Sci.*, 2012, **24**, 757–764.

40 H. Bao, X. Chen, J. Fang, Z. Jiang and W. Huang, *Catal. Letters*, 2008, **125**, 160–167.

41 J. Wang, M. Shen, J. Wang, M. Cui, J. Gao, J. Ma and S. Liu, *J. Environ. Sci.*, 2012, **24**, 757–764.

42 L. Atzori, M. G. Cutrufello, D. Meloni, R. Monaci, C. Cannas, D. Gazzoli, M. F. Sini, P. Deiana and E. Rombi, *Int. J. Hydrogen Energy*, 2017, **42**, 20689–20702.

43 H. Yang, X. Mao, Y. Guo, D. Wang, G. Ge, R. Yang, X. Qiu, Y. Yang, C. Wang, Y. Wang and G. Liu, *CrystEngComm*, 2010, **12**, 1842–1849.

44 P. H. Bolt, F. H. P. M. Habraken and J. W. Geus, *J. Solid State Chem.*, 1998, **135**, 59–69.

45 W. K. Jozwiak, E. Kaczmarek, T. P. Maniecki, W. Ignaczak and W. Maniukiewicz, *Appl. Catal. A Gen.*, 2007, **326**, 17–27.

46 E. Bêche, P. Charvin, D. Perarnau, S. Abanades and G. Flamant, *Surf. Interface Anal.*, 2008, **40**, 264–267.

47 X. Wang, J. A. Rodriguez, J. C. Hanson, D. Gamarra, A. Martinez-Arias and M. Fernandez-Garcia, *J. Phys. Chem. B*, 2006, **110**, 428–434.

48 T. Yamashita and P. Hayes, *Appl. Surf. Sci.*, 2008, **254**, 2441–2449.

49 A. Álvarez, M. Borges, J. J. Corral-Pérez, J. G. Olcina, L. Hu, D. Cornu, R. Huang, D. Stoian and A. Urakawa, *ChemPhysChem*, 2017, **18**, 3135–3141.

50 K. R. Hahn, M. Iannuzzi, A. P. Seitsonen and J. Hutter, *J. Phys. Chem. C*, 2013, **117**, 1701–1711.